RSC Advances

ROYAL SOCIETY OF CHEMISTRY

www.rsc.org/advances

Palladium-loaded magnetic core–shell porous carbon nanospheres derived from metal–organic framework as a recyclable catalyst

Chao Bao, Lincheng Zhou*, Yanming Shao, Qiong Wu, Junjun Ma, He Zhang

State Key Laboratory of Applied Organic Chemistry, College of Chemistry and Chemical Engineering, Institute of Biochemical Engineering & Environmental Technology, Lanzhou University, Lanzhou 730000, P. R. China

Chao Bao E-mail: baoch13@lzu.edu.cn Fax: 86-931-8912113 Tel. 86-931-8912528
Address: College of Chemistry and Chemical Engineering, Lanzhou University, Lanzhou 730000, P.R.China

Lincheng Zhou E-mail: zhoulc@lzu.edu.cn Fax: 86-931-8912113 Tel. 86-931-8912528
Address: College of Chemistry and Chemical Engineering, Lanzhou University, Lanzhou 730000, P.R.China

Yanming Shao E-mail: shaoym11@lzu.edu.cn Fax: 86-931-8912113 Tel. 86-931-8912528
Address: College of Chemistry and Chemical Engineering, Lanzhou University, Lanzhou 730000, P.R.China

Qiong Wu E-mail: qwu14@lzu.edu.cn Fax: 86-931-8912113 Tel. 86-931-8912528
Address: College of Chemistry and Chemical Engineering, Lanzhou University, Lanzhou 730000, P.R.China

Junjun Ma E-mail: majj12@lzu.edu.cn Fax: 86-931-8912113 Tel. 86-931-8912528
Address: College of Chemistry and Chemical Engineering, Lanzhou University, Lanzhou 730000, P.R.China

He Zhang E-mail: zhangh12@lzu.edu.cn Fax: 86-931-8912113 Tel. 86-931-8912528
Address: College of Chemistry and Chemical Engineering, Lanzhou University, Lanzhou 730000, P.R.China

*Corresponding author. Tel: 86-931-8912528. E-mail: Zhoulc@lzu.edu.cn (Zhou lincheng)

Abstract

Separation and recycling of noble metal nanocatalysts after catalytic reactions are significant challenges to reduce catalyst cost and avoid waste generation in industrial applications. In this study, Pd-loaded magnetic porous carbon nanospheres (Fe_3O_4@MC-Pd) were prepared by annealing Fe_3O_4@MIL-100/$PdCl_2$, which was fabricated through a facile one-pot solvothermal method, at 450°C in nitrogen atmosphere. The novel Fe_3O_4@MC-Pd catalyst consists of a superparamagnetic Fe_3O_4 core and a chemical inertness porous carbon layer, which can protect the Fe_3O_4 core from extreme external environment and prevent the loss of Pd NPs. The resultant composite material showed excellent catalytic performance in reducing methylene blue with sodium borohydride as reducing agent and superparamagnetic behavior that enabled the magnetic separation and convenient recovery of the nanocatalysts from the reaction mixture. Moreover, the composite material also showed good thermal and acid stability, fast regeneration ability, and high cyclic stability (>10 cycles without loss of catalytic efficiency). The result shows the nanocatalysts could overcome the drawbacks of MOF catalysts (chemical unstability). This study indicated that the as-prepared Fe_3O_4@MC-Pd composite material shows great potential for using in a wide range of applications.

1. Introduction

Noble metal nanoparticles (NMNPs), such as Pt, Au, Ag, and Pd, have attracted increasing attention owing to their high catalytic activities toward different types of reactions.[1–8] Thus, they are considered excellent candidates for the design of highly active catalysts. However, aggregation of metal nanoparticles (NPs), which is the main obstacle in the use of catalytic NPs in real application, severely reduce the catalytic efficiency of the catalysts.[9,10] Moreover, recycling NPs is a complicated task because they are too small.[11] Thus, the stability and separation of the NMNPs are two crucial issues for their further applications.

To solve the stability problem, various techniques have been developed, such as stabilizing NPs by ligands and embedding NPs inside shells.[12,13] Among these strategies, the immobilization of NMNPs on solid supports has been regarded as the most frequently used approach to preserve their catalytic properties.[14–19] In this strategy, aggregation of noble NPs can be prevented efficiently by dispersing noble NPs finely on the support.[20,21] The emergence of new nanomaterials, such as carbon-based materials (graphene oxide, carbon nanotubes, and carbon nanobers),[22,23] mesoporous silica,[24] polymers,[25–29] and metal oxides,[30,31] provides promising support in fabrication of composite catalysts. Among a variety of catalyst supports, carbonaceous materials, such as graphene, carbon nanotubes, and active carbons, exhibit remarkable advantages owing to their excellent chemical stability, mechanical strength, and large surface area.[32,33] However, NMNPs that are physically attached to carbonaceous materials leach easily during catalytic process, which causes a

significant loss of catalytic activity. Only functionalized with O- and N-containing functional groups, the NMNPs on these carbonaceous materials cannot be easily leached and subsequently maintain high cyclic stability.[34]

Metal–organic frameworks (MOFs) are crystalline materials composed of metal ions and organic ligands. The pore size and functional groups of MOFs can be adjusted given the enormous variety of metal ions and organic ligands.[35–37] These distinct characteristics make them excellent candidates for various applications, such as gas storage,[38,39] sensing,[40] chemical separation,[41] drug delivery,[42] and catalysis.[43] In recent years, utilization of MOFs as heterogeneous catalysts has received remarkable attention. However, application of MOFs in special environments, such as acid, alkali, and high temperature, is limited because of their low stability. Moreover, recycling MOFs is a complicated task after reaction. Utilization of MOFs as templates or precursor materials to produce porous carbonaceous materials has been demonstrated by taking advantage of the fact that MOFs have large surface area and possess a significant amount of carbon source.[44,45] Meanwhile, to solve the separation problem, magnetic nanomaterials may be adopted as catalyst supports because they exhibit remarkable advantages owing to their easy separation for reuse by applying an external magnetic field. In addition, the use of magnetic separation can reduce the capital and operational costs.

In this paper, we report a facile method to synthesize Fe_3O_4@MC-Pd composite material derived from Fe_3O_4@MIL-100(Fe)/$PdCl_2$ at 450°C in nitrogen atmosphere. First, Fe_3O_4 nanospheres were prepared through a traditional hydrothermal method,

and then the nanospheres were modified by carboxylic acid. Subsequently, Fe_3O_4@MIL-100(Fe) was prepared using the modified Fe_3O_4 NPs as templates through a one-pot self-assembly strategy. The resultant composite not only has excellent morphology but also shows a high Brunauer–Emmett–Teller (BET) surface area. Finally, the as-synthesized Fe_3O_4@MIL-100(Fe) was added to ethanol solution of the precursor (H_2PdCl_4) with constant vigorous stirring. The magnetic porous carbon (MPC) that contains Pd (Fe_3O_4@MC-Pd) composite was prepared by annealing Fe_3O_4@MIL-100 (Fe)/$PdCl_2$ in nitrogen atmosphere. Both one-pot self-assembly strategy for Fe_3O_4@MIL-100(Fe) preparation and one-step synthesis of Fe_3O_4@MC-Pd from Fe_3O_4@MIL-100(Fe)/$PdCl_2$ have rarely been reported.

The catalytic activity of the as-prepared Fe_3O_4@MC-Pd in reduction of methylene blue (MB) with $NaBH_4$ was evaluated. Compared with other methods of magnetic-Pd catalyst formation, additional toxic reagent is unnecessary in the present method. The Fe_3O_4@MC-Pd exhibits excellent catalytic activity compared with most of the other reported catalysts. The as-synthesized nanocatalyst shows high efficiency in magnetic separation and recovery because of the high saturation magnetization and super-paramagnetic property. In addition, the chemical and thermal stability of Fe_3O_4@MC-Pd materials are better than those of Fe_3O_4@MIL-100(Fe). These advantages make Fe_3O_4@MC-Pd materials an excellent catalyst for practical application.

2. Experimental

2.1 Materials

Sodium citrate and $FeCl_3$ were purchased from Sinopharm Chemical Reagent Co. (Shanghai,China). Benzene-1,3,5-tricarboxylicacid (H_3btc) and (3-aminopropyl) triethoxysilane (APTES) were purchased from Aldrich. Succinic anhydride and sodium hydroxide were purchased from Shanghai Chemical Reagents Company. Ethylene glycol was supplied by Tianjin Fine Chemicals Co., Ltd. Palladium chloride ($PdCl_2$) were purchased from Sigma Aldrich. All the chemicals were of analytical grade.

2.2 Synthesis of Fe_3O_4 NPs

Fe_3O_4 NPs were prepared via a one-pot hydrothermal method.[46] In a typical experiment, 2.6 g of anhydrous $FeCl_3$ and 1.0 g of trisodium citrate dihydrate were first dissolved in 80 mL of ethylene glycol under vigorous stirring for 30 min. Then, 4.0 g of NaAc was added while stirring for 30 min. The mixture was then sealed in a Teflon-lined stainless-steel autoclave and heated at 200°C for 10 h. Afterward, the autoclave was carefully removed and allowed to cool to room temperature. The products were separated and washed with ultrapure water and ethanol for several times and dried under vacuum at 50°C.

2.3 Preparation of COOH-functionalized Fe_3O_4 microspheres

Fe_3O_4 NPs were first modified by APTES, which was achieved by adding 160 mL of ethanol, 40 mL of deionized water, 3 mL of $NH_3 \cdot H_2O$, and 1.2 g of APTES into a three-necked round-bottom flask, which was equipped with a mechanical stirrer. Moreover, the mixture was vigorously stirred for 24 h at 60°C. Then, the obtained Fe_3O_4/APTES microspheres were collected through magnetic separation and washed

with ethanol for several times to remove excess APTES. The resultant Fe_3O_4/APTES NPs were dried in a vacuum oven at 50°C until constant weight was achieved. Then, 200 mg of Fe_3O_4/APTES and 200 mg of succinic anhydride were dispersed in 60 mL of DMF solution and stirred for 24 h at room temperature. The solid products were collected with an external magnetic field, rinsed with ultrapure water and ethanol for several times, and finally dried under vacuum at 50°C for further use.

2.4 Preparation of core–shell magnetic Fe_3O_4@MIL-100(Fe) microspheres

The magnetic Fe_3O_4@MIL-100(Fe) microspheres were fabricated through a one-pot assembly strategy. The COOH-functionalized Fe_3O_4 microspheres (250 mg) were obtained and dispersed in 30 mL of ethanol solution. Then, 50 mL of DMF containing $FeCl_3$ (500 mg) and 1,3,5-benzenetricarboxylic acid (H_3BTC) (300 mg) was added. Finally, the mixture was transferred into a Teflon-lined stainless-steel autoclave with a capacity of 100 mL and was heated at 120°C for 24 h. After cooling to room temperature, the solid products were collected from the solution with the use of an external magnet. The solid products were washed with water for several times and dried in a vacuum at 60°C.

2.5 Synthesis of Fe_3O_4@MC-Pd microspheres

Fe_3O_4@MC-Pd microspheres were synthesized through a one-step strategy. The as-synthesized Fe_3O_4@MIL-100(Fe) (50 mg) was typically added to 10 mL of ethanol solution containing H_2PdCl_4 (25 μmol) with constant vigorous stirring for 6 h. The resultant Fe_3O_4@MIL-100 (Fe)/$PdCl_2$ microspheres were then recovered with a magnet and dried in a vacuum oven at 50°C until constant weight was achieved.

Finally, the Fe_3O_4@MC-Pd microspheres were prepared by annealing Fe_3O_4@MIL-100(Fe)/$PdCl_2$ at 450°C in nitrogen atmosphere for 1 h. After cooling to room temperature, the as-prepared Fe_3O_4@MC-Pd microspheres were collected.

2.6 Catalysis test

The catalytic property of Fe_3O_4@MC-Pd materials was investigated in terms of the absorbance intensity change at the maximum absorbance wavelength of the MB dye. Typically, 2.75 mL of ultrapure water and an aqueous solution (200 μL) of freshly prepared $NaBH_4$ (100 mM) were added to a solution (25 μL) of MB (100 mM), respectively. Subsequently, 25 μL of aqueous dispersion of the catalyst (1 mg/mL) was added to start the reaction. Then, the blue solution gradually faded as the reaction proceeded, which could be observed by the naked eye. The progress of the conversion reaction was monitored by measuring the changes in absorbance at 665 nm with a UV-vis spectrophotometer.

2.7 Stability Tests

A 10 mg portion of Fe_3O_4@MC-Pd microspheres was dispersed in 20 mL of boiling water and kept for 10 h to test the stability of the catalyst. Another 10 mg portion of Fe_3O_4@MC-Pd microspheres was dispersed in 10 mL of hydrochloric acid solution at pH 2 for 24 h to test the acid stability of the sample.

The recyclability of Fe_3O_4@MC-Pd microspheres for MB reduction was also investigated for 10 cycles. After each run, the solid catalyst was recovered with a magnet, washed with water and ethanol, and dried under vacuum. To evaluate the stability, the conversions were determined via UV-vis detection of the residual MB in

the mixture after reaction. Furthermore, Pd wt.% was also measured with ICP-AES for every cycle.

2.8 Characterization

The morphology of the sample was examined by transmission electron microscope (TEM, TecnaiG2F30) and scanning electron microscope (SEM, JSM-6701F, JEOL, Japan).. FT-IR spectra were obtained in transmission mode on a FT-IR spectrometer (American Nicolet Corp., Model 170-SX) using the KBr pellet technique. XRD (Rigaku D/MAX-2400 X-ray diffractometer with Ni-filtered Cu Kα radiation (λ = 1.54056)) was used to investigate the crystal structure of the nanoparticles. The Pd content of the prepared nanocatalysts were obtained by inductively coupled plasma atomic emission spectroscopy (ICP-AES). Magnetization measurements at room temperature were obtained using a Vibrating sample magnetometer (LAKESHORE-7304, USA) at room temperature. The X-ray photoelectron spectroscopy (XPS) spectra were obtained with an ESCALab220i-XL electron spectrometer (VG Scientific) using 300 W Al-Kα radiation. The N_2 adsorption-desorption isotherm was measured at liquid nitrogen temperature (77 K) using a Micromeritics ASAP 2020 analyzer. The specific surface area was calculated by the BET method. The pore size distribution was obtained using the Barret-Joner-Halenda (BJH) method. UV-Vis detection was carried out on a TU-1810PC UV-Vis spectrophotometer (Purkinje General, China).

3. Results and discussion

3.1 Morphology and structure characterization

Fig. 1 outlines the procedure to prepare Fe_3O_4@MC-Pd microspheres. Initially,

Fe_3O_4 NPs were synthesized via a robust solvothermal method. Then, the NPs were modified with carboxylic acid. Fe_3O_4@MIL-100 was prepared using the modified Fe_3O_4 NPs as templates through a one-pot self-assembly strategy. Finally, the Fe_3O_4@MC-Pd composite was prepared by annealing Fe_3O_4@MIL-100(Fe)/$PdCl_2$ in nitrogen atmosphere. The TEM (Fig. 2A) and SEM (Figs. 2E, 2J) images show that the obtained magnetite particles are nearly spherical and have an average diameter of approximately 250 nm. Subsequently, magnetic Fe_3O_4@MIL-100(Fe) microspheres were then fabricated by a one-pot assembly strategy. Fig. 2 shows representative TEM (Fig. 2B) and SEM (Figs. 2F, 2K) images of the microspheres. The diameter of the Fe_3O_4@MIL-100 microspheres was approximately 450 nm. In the one-pot assembly strategy, DMF is used as the solvent for H_3BDC solution and it directly determines whether MIL-100 (Fe) can be produced. Ethanol is also vital for the formation of core–shell NPs. Its presence can change the coordination environment of metal ions such that MIL-100(Fe) grows preferentially around Fe_3O_4 NPs instead of self-nucleating in solution.[47] The Fe_3O_4@MC-Pd microspheres prepared by annealing Fe_3O_4@MIL-100/$PdCl_2$ at 450°C under nitrogen atmosphere also showed excellent morphology, and the diameter was approximately 400 nm (Figs. 2C, 2G, 2H). The Pd nanoparticles randomly disperse in the porous carbon layer of Fe_3O_4@MC-Pd microspheres. Their size distribution was evaluated statistically through measuring the diameter of 150 Pd nanoparticles in the TEM images. it can be seen that the particle size of Pd distributes mainly between 1.0 nm and 7.0 nm with an average diameter of about 5.0 nm (Fig. 3), which are small enough to be accommodated in the

mesoporous cavities of the Fe_3O_4@MC-Pd microspheres. Furthermore, utilizing N_2 reduction can effectively avoid aggregation of metal NPs. Fig. 4 shows high-angle annular dark-field scanning transmission electron microscopy (HAADF-STEM) images that display a detailed elemental distribution of the nanocatalysts. The figures clearly demonstrate that Fe_3O_4@MC-Pd is mainly composed of C, O, Fe, and Pd elements. Moreover, the Pd mapping image (Fig. 4E) shows that the Pd NPs are distributed well in the spaces of porous carbon layer compared with the prepared MPC nanocatalysts described in Ma *et al*.[48]

Surface modification of Fe_3O_4 microspheres and further functionalized microspheres with –COOH was investigated via FTIR spectroscopy (Fig. 5). The absorption peaks for the Fe_3O_4 microspheres at 455 and 578 cm^{-1} can be assigned to the vibrations of the Fe-O functional group, which corresponded to reported stretching vibrations of Fe-O in bulk Fe_3O_4.[49] The peaks at 3415 cm^{-1} is caused by the stretching vibrations of N–H. Moreover, 1440 and 1562 cm^{-1} are caused by the stretching vibrations of C=C in benzene ring, whereas the peaks at 1371 and 1619 cm^{-1} are attributed to C=O stretching vibrations of carboxylic acid, thereby suggesting that MIL-100 shell has been successfully coated on the surface of Fe_3O_4.

PXRD analysis also provided information regarding the composition of the as-synthesized samples. To verify the formation of Fe_3O_4@MC-Pd microspheres, XRD patterns of Fe_3O_4, Fe_3O_4@MIL-100(Fe), and Fe_3O_4@MC-Pd samples were obtained, as shown in Fig. 6. The diffraction peaks of the Fe_3O_4@MIL-100(Fe) microspheres and Fe_3O_4@MC-Pd at 2θ = 30.0°, 35.5°, 43.2°, 53.8°, 57.2°, and 62.6°

were ascribed to (220), (311), (400), (422), (511), and (440) planes, which agree well with the standard XRD data for the cubic phase Fe_3O_4 (JCPDS card, file no. 89-4319), with a face-centered cubic structure.[50] In addition to these peaks of Fe_3O_4@MIL-100(Fe), additional peaks exist at 3.4° (022), 3.9° (113), 5.3° (333), 11° (428), 14.2° (088), 18.2° (7911), 20.1° (4814), 24° (6618), and 27.7° (9321), which correspond to the crystalline MIL-100, as reported previously.[51] This finding demonstrates the formation of the crystal Fe_3O_4@MIL-100(Fe). After carbonization process, some diffraction peaks, which belong to crystal MIL-100, had disappeared. However, the weak diffraction (111) reflections of typical cubic Pd NPs were detected, which indicate the formation of very small Pd NPs.[52] These observations match well with TEM observations. The XRD results indicated that the metal precursors are successfully reduced to metallic NPs.

XPS was employed to verify the composition of the resulting hybrid magnetic microspheres by investigating the chemical state of the surface of obtained Fe_3O_4@MC-Pd microspheres. Fig. 7A exhibits the overall surveys of the as synthesized Fe_3O_4@MC-Pd microspheres, which clearly show the signals of elemental C, O, and Fe. Fig. 7A clearly illustrates that the signal of C is much stronger than that of other elements (i.e., O, Pd, and Fe) on the surface of the nanocatalysts. This phenomenon results from carbonization process, which is in accordance with the TEM observations. In addition, Fig. 7B shows the XPS spectra of Pd 3d. The peaks at 335.8 and 341.2 eV are assigned to Pd $3d_{5/2}$ and Pd $3d_{3/2}$, respectively. The position of the Pd 3d peaks corresponds to Pd^0, which is in good

agreement with that described in the previous literature.[53] According to these spectra, all of the metal ions are reduced to NMNPs after carbonization process. The Fe 2p spectrum can be deconvoluted into two peaks centered at 725.2 and 711.1 eV, which correspond to the peaks of Fe $2p_{1/2}$ and Fe $2p_{3/2}$ (Fig. 7C). The position of the Fe 2p peaks corresponds to that of Fe_2O_3 or Fe_3O_4.[54] The C 1s peak at 284.6 eV (Fig. 7D) corresponds to C-C/C=C species.[55]

The shell also contained iron oxide after carbonization process. Thus, to analyze the composition of iron oxide, MS is indispensable. Fig. 8 shows that the spectrum was interpreted by two sextets and one doublet. The two sextets (Heff = 47.96 and 45.31 T and IS = 0.32 and 0.25 mm s^{-1}) belong to magnetite,[56] which accounts for 81.60%. The doublet accounting for 18.5% with IS = 0.39 mm s^{-1} and QS = 0.81 mm s^{-1} may be Fe_2O_3,[57] which corresponds to the analysis of XPS.

The BET surface area were measured using the N_2 adsorption/desorption isotherms at −197.2°C. Before measurements, the samples were evacuated at 100 °C for 10 h. The BET surface area, pore volume, and adsorption average pore width (Fig. S1) of Fe_3O_4@MIL-100(Fe) are 505.09 m^2/g, 0.53 cm^3/g, and 4.16 nm, respectively. The surface areas of the samples obtained via the one-pot assembly strategy are higher and their pore sizes are larger than those prepared via the step-by-step assembly strategy. Thus, the one-pot assembly strategy is beneficial for diffusion of the metallic precursors into the pores. After carbonization, the BET surface areas and pore volumes of Fe_3O_4@MC-Pd are only 51.47 m^2/g and 0.078 cm^3/g, respectively. Compared with Fe_3O_4@MIL-100(Fe), the surface areas and the pore volumes of

Fe_3O_4@MC-Pd had considerably decreased. The results indicated that the structure is partly damaged in the carbonization process, and the pores of the host frameworks are occupied by dispersed Pd NPs. However, the adsorption average pore width of the nanocatalysts increased to 6.06 nm, which provides valuable sites for catalytic reaction.

The magnetic properties of the resultant core–shell microspheres were investigated at room temperature with vibrating sample magnetometry in the field range of −10 kOe to 10 kOe (Fig. 9). The magnetization saturation values of Fe_3O_4, Fe_3O_4@MIL-100(Fe), and Fe_3O_4@MC-Pd were measured as 69.5, 22.7, and 60.4 emu/g, respectively, which are much higher than the value in literature (i.e., 45.07 emu/g) with Fe_3O_4@Pd/MIL-100(Fe) as nanocatalysts.[58] The measured values indicated the strong magnetic properties of the prepared nanocatalysts. All of the curves present a magnetic hysteresis loop, which also depicts the strong magnetic response to a varying magnetic field. Furthermore, Fe_3O_4, Fe_3O_4@MIL-100(Fe), and Fe_3O_4@MC-Pd indicated ferromagnetic-type curves, which show a hysteresis loop. The values of coercivity and remanence are summarized in Table 1. Fast aggregation of the nanocatalysts can be observed from their homogeneous dispersion in the presence of an external magnetic field applied for 10 s. This observation directly demonstrates the convenient separation of the nanocatalysts through an external magnetic field, which is important in terms of their practical manipulation.

3.2. Catalytic Reduction Tests

Metallic Pd nanostructures have been demonstrated as excellent catalysts with

high activity and selectivity.[59,60] In the current investigation, the catalytic performance of Fe_3O_4@MC-Pd microspheres for reduction of MB with $NaBH_4$ was investigated. The main merit for the reduction of MB with $NaBH_4$ is its convenient monitoring via UV-vis absorption spectroscopy, given that no side reactions exist. Fig. 10 depicts the performance of the Fe_3O_4@MC-Pd microspheres as catalysts in the reduction of MB by $NaBH_4$. The Fe_3O_4@MC-Pd microspheres serve as millions of nanoreactors, where the reduction actions take place via relaying electrons from the donor BH_4^- to the acceptor MB. In aqueous medium BH_4^- is adsorbed onto the surface of the catalyst. The hydrogen atom, which is formed from the hydride, after electron transfer to the noble metallic NPs, attacks MB molecules to reduce it.

The progress of the catalytic reduction of MB can be easily followed by the decrease in absorbance at λ_{max} of MB with time. Fig. 11A shows the successive UV-vis spectra of MB in the presence of Fe_3O_4@MC-Pd and $NaBH_4$ in aqueous solution. A control experiment was conducted with Fe_3O_4@MC-Pd as the catalysts to clarify the catalytic effect of NPs. To elucidate the reaction mechanism, the concentration of $NaBH_4$ can be considered constant throughout the reaction, given that it was in a considerable excess. Therefore, pseudo-first-order kinetics with regard to the catalytic reduction of MB, described as $\ln(C/C_0) = -kt$, can be applied, where C is the concentration of MB at time t, C_0 is the initial concentration of MB, and k is the rate constant. Fig. 11B reveals the linear relationship between $\ln(C/C_0)$ and the reaction time t, which matches well with the first-order reaction kinetics. The rate constant, k, of MB catalytic reduction is calculated as 5.97 min^{-1} at 25°C for the case

with Fe_3O_4@MC-Pd microspheres, which is much larger than that reported by the literature, that is, 0.430 min^{-1} with Fe_3O_4@PDA-Ag as catalyst,[61] 0.266 min^{-1} with Au@polypyrrole/Fe_3O_4 hollow capsules as nanocatalyst,[53] and 0.05 min^{-1} with Ag NP-embedded hybrid microgels as catalyst.[62] Therefore, the catalytic activity of as-synthesized catalysts in the present work is higher than that of most of the other catalysts. This outstanding catalytic performance can be ascribed to the high loading amount and well distributing of Pd NPs in the developed microspheres. The inset photos in Fig. 11 show that the colors of MB + $NaBH_4$ are different in the absence of catalyst (A) and in the presence of Fe_3O_4 (B), Fe_3O_4@MC (C), and Fe_3O_4@MC-Pd (D). The first three solutions almost maintain the same colors. However, by adding a small amount of Fe_3O_4@MC-Pd, the color of MB solution changed in only several seconds, thereby indicating that the reduction of MB via $NaBH_4$ occurs very fast in the presence of Fe_3O_4@MC-Pd. The superior catalytic performance of Fe_3O_4@MC-Pd microspheres confirms that the composite microspheres can serve as excellent supports for NMNPs.

To evaluate the pH effect of the MB solution on the catalytic activity of Fe_3O_4@MC-Pd microspheres, MB solutions with three different pH values (pH 3, 7, 9) were used for the tests. Figure 12A-C shows that there is no significant change on the catalytic activity of Fe_3O_4@MC-Pd microspheres under different pH conditions, which implies that the high catalytic activity of the microspheres could withhold in various solution conditions of different pHs. The MOFs is effective only within a low and narrow pH range due to its chemical unstability, but the Fe_3O_4@MC-Pd

microspheres resulted in a broader pH range.

In addition, the reduction of 4-Nitrophenol (4-NP) with $NaBH_4$ has also been used as another model reaction to check the catalytic activity of the as-prepared Fe_3O_4@MC-Pd microspheres. Fig. S2 shows the successive UV-vis spectra of 4-NP in the presence of Fe_3O_4@MC-Pd microspheres and $NaBH_4$ in aqueous solution. The color of the 4-NP solution vanishes gradually, indicated by the gradual decrease in absorbance value at 400 nm. Meanwhile, a new peak centered at 296 nm appears and increases with reaction time. This peak could be indexed to the characteristic absorbance peak of 4-AP, further confirming the reduction of 4-NP to 4-AP. Therefore, the Fe_3O_4@MC-Pd microspheres exhibit the potential application as an effective catalyst for the reduction of various organic dyes.

3.3. Stability Tests

Stability of Fe_3O_4@MC-Pd microspheres is a critical factor for their practical applications. In this work, the catalyst maintained the same morphology as that of fresh samples after 10 h in boiling water (Fig. 13A). Meanwhile, given that Fe_3O_4 microspheres can be easily etched under acid conditions, the acid stability of Fe_3O_4@MC-Pd microspheres was also tested under a strong acid environment (pH 2) for over 24 h. The TEM images (Fig. 13B) showed that the Fe_3O_4@MC-Pd microspheres maintain the core−shell structure under strong acid condition. The catalyst also maintained the same morphology under a strong alkali environment (pH 12) for over 24 h (Fig. 13C). Furthermore, the ICP-AES results (Table 2) confirmed that the catalyst can withstand the strong acid and alkali condition. Therefore, the

robust C layer can effectively protect Fe_3O_4 cores, bind the Pd NPs under strong acid and alkali conditions, and show good stability in practical applications.

Recyclability of the as-prepared catalyst was also evaluated. The catalytic activity remains stable even after 10 cycles, and the conversion of each cycle remains nearly 100% (Fig. 14). In addition, no changes were found in the XPS spectra of the microspheres after 10 reduction cycles (Fig. S3), which confirms the long-term stability of the nanocatalysts. This high stability can be attributed to the core–shell porous architecture of the as-prepared microspheres, which provides both docking sites for MB and a superparamagnetic core that allows easy manipulation by a magnet. The solid catalyst was magnetically separated from the reactant mixture after each catalytic cycle. The residual solution was collected and measured by ICP-AES to determine the loss of Fe and Pd. The results showed that no Fe element was determined in residual solution and only trace amounts of Pd element was detected in the residual solution. As shown in Fig. 15, nearly 80% of Pd content was maintained on the catalyst even after 10 cycles. These results suggested that the solid catalyst has high stability.

4. Conclusion

In conclusion, a facile and efficient approach to prepare Fe_3O_4@MC-Pd microspheres was developed. The resultant composite material showed excellent catalytic performance in reduction of MB and superparamagnetic behavior that enabled magnetic separation and convenient recovery of the nanocatalysts from the reaction mixture. Moreover, the composite catalysts showed good thermal and acid

stability, fast regeneration ability, and high cyclic stability, indicating that it could overcome the drawbacks of MOF catalysts (chemical unstability). This study may aid in the further development of effective reducation catalysts for organic reactions. Therefore, the composite catalysts show great potential for industrial application.

Acknowledgement

The authors would like to express their appreciation for research funding provided by the National Natural Science Foundation of China (Nos. 21374045, 21074049) and the National Science Foundation for Fostering Talents in Basic Research of the National Natural Science Foundation of China (Grant No. J1103307).

References

1. S. B. Kalidindi and B. R. Jagirdar, *ChemSusChem* **2012,** *5* , 65-75.
2. M. S. Yavuz, Y. Cheng, J. Chen, C. M. Cobley, Q. Zhang, M. Rycenga, J. Xie, C. Kim, K. H. Song, A. G. Schwartz, L. V. Wang and Y. Xia, *Nat. Mater.* **2009,** *8*, 935-939.
3. N. Tian, Z.-Y. Zhou, S.-G. Sun, Y. Ding and Z. L. Wang, *Science* **2007,** *316* , 732-735.
4. B. Lim, M. Jiang, P. H. C. Camargo, E. C. Cho, J. Tao, X. Lu, Y. Zhu and Y. Xia, *Science* **2009,** *324* , 1302-1305.
5. H. Lee, S. E. Habas, S. Kweskin, D. Butcher, G. A. Somorjai and P. Yang, *Angew. Chem. Int. Ed.* **2006,** *45*, 7824-7828.
6. Y. Xia, Y. Xiong, B. Lim and S. E. Skrabalak, *Angew. Chem. Int. Ed.* **2009,** *48*, 60-103.
7. C. Burda, X. Chen, R. Narayanan and M. A. El-Sayed, *Chem. Rev.* **2005,** *105*, 1025-1102.
8. S. E. Skrabalak, J. Chen, Y. Sun, X. Lu, L. Au, C. M. Cobley and Y. Xia, *Acc. Chem. Res.* **2008,** *41*, 1587-1595.
9. Y. Lin, Y. Qiao, Y. Wang, Y. Yan and J. Huang, *J. Mater. Chem.* **2012,** *22*, 18314-18320.
10. M. Zhao, K. Deng, L. He, Y. Liu, G. Li, H. Zhao and Z. Tang, *J. Am. Chem. Soc.* **2014,** *136*, 1738-1741.
11. C. César, L. S. Jonathan and A. André, *J. Phys. D: Appl. Phys.* **2013,** *46*, 362001.
12. Y. Song, A. S. Harper and R. W. Murray, *Langmuir* **2005,** *21*, 5492-5500.
13. S. Fujii, A. Aichi, K. Akamatsu, H. Nawafune and Y. Nakamura, *J. Mater. Chem.* **2007,** *17*, 3777-3779.
14. B. J. Gallon, R. W. Kojima, R. B. Kaner and P. L. Diaconescu, *Angew. Chem. Int. Ed.***2007,** *46*, 7251-7254.
15. C. Zhu, L. Han, P. Hu and S. Dong, *Nanoscale* **2012,** *4*, 1641-1646.

16. Y. Deng, Y. Cai, Z. Sun, J. Liu, C. Liu, J. Wei, W. Li, C. Liu, Y. Wang and D. Zhao, *J. Am. Chem. Soc.* **2010,** *132*, 8466-8473.
17. Z. Sun, B. Sun, M. Qiao, J. Wei, Q. Yue, C. Wang, Y. Deng, S. Kaliaguine and D. Zhao, *J. Am. Chem. Soc.* **2012,** *134*, 17653-17660.
18. J. Ge, Q. Zhang, T. Zhang and Y. Yin, *Angew. Chem. Int. Ed.* **2008,** *47*, 8924-8928.
19. T. Yu, J. Zeng, B. Lim and Y. Xia, *Advanced Materials*, *Adv. Mater.* **2010,** *22*, 5188-5192.
20. M. S. Chen and D. W. Goodman, *Science* **2004,** *306*, 252-255.
21. A. A. Herzing, C. J. Kiely, A. F. Carley, P. Landon and G. J. Hutchings, *Science* **2008,** *321*, 1331-1335.
22. R. Liu, S. M. Mahurin, C. Li, R. R. Unocic, J. C. Idrobo, H. Gao, S. J. Pennycook and S. Dai, *Angew. Chem. Int. Ed.* **2011,** *123*, 6931-6934.
23. H. Li, J. K. Jo, L. Zhang, C.-S. Ha, H. Suh and I. Kim, *Adv. Funct. Mater.* **2010,** *20*, 3864-3873.
24. Y. H. Kim, S.-D. Yim and E. D. Park, *Catal. Today* **2012,** *185*, 143-150.
25. G. L. Li, L. Q. Xu, K. G. Neoh and E. T. Kang, *Macromolecules* **2011,** *44*, 2365-2370.
26. A. M. Signori, K. d. O. Santos, R. Eising, B. L. Albuquerque, F. C. Giacomelli and J. B. Domingos, *Langmuir* **2010,** *26*, 17772-17779.
27. Y. Mei, Y. Lu, F. Polzer, M. Ballauff and M. Drechsler, *Chem. Mater.* **2007,** *19*, 1062-1069.
28. Y. Mei, G. Sharma, Y. Lu, M. Ballauff, M. Drechsler, T. Irrgang and R. Kempe, *Langmuir* **2005,** *21*, 12229-12234.
29. X. Zhang and Z. Su, *Adv. Mater.* **2012,** *24*, 4574-4577.
30. Z. W. Seh, S. Liu, M. Low, S.-Y. Zhang, Z. Liu, A. Mlayah and M.-Y. Han, *Adv. Mater.* **2012,** *24*, 2310-2314.
31. M. Haruta, *CATTECH* **2002,** *6*, 102-115.
32. B. Qiao, A. Wang, X. Yang, L. F. Allard, Z. Jiang, Y. Cui, J. Liu, J. Li and T. Zhang, *Nat Chem* **2011,** *3*, 634-641.
33. G. Özkan, S. Gök and G. Özkan, *Chem. Eng. J.* **2011,** *171*, 1270-1275.
34. X. Wan, C. Zhou, J. Chen, W. Deng, Q. Zhang, Y. Yang and Y. Wang, *ACS Catalysis* **2014,** *4*, 2175-2185.
35. B. Xia, Y. Yan, X. Wang and X. W. Lou, *Materials Horizons* **2014,** *1*, 379-399.
36. H.-C. Zhou, J. R. Long and O. M. Yaghi, *Chem. Rev.***2012,** *112*, 673-674.
37. D. Bradshaw, J. B. Claridge, E. J. Cussen, T. J. Prior and M. J. Rosseinsky, *Acc. Chem. Res.* **2005,** *38*, 273-282.
38. M. O'Keeffe, M. A. Peskov, S. J. Ramsden and O. M. Yaghi, *Acc. Chem. Res.* **2008,** *41*, 1782-1789.
39. N. L. Rosi, J. Eckert, M. Eddaoudi, D. T. Vodak, J. Kim, M. O'Keeffe and O. M. Yaghi, *Science* **2003,** *300*, 1127-1129.
40. O. K. Farha, A. Özgür Yazaydın, I. Eryazici, C. D. Malliakas, B. G. Hauser, M. G. Kanatzidis, S. T. Nguyen, R. Q. Snurr and J. T. Hupp, *Nat Chem* **2010,** *2*, 944-948.
41. C.-X. Yang, H.-B. Ren and X.-P. Yan, *Anal. Chem.* **2013,** *85*, 7441-7446.
42. Y. Hu, Z. Huang, J. Liao and G. Li, *Anal. Chem.* **2013,** *85*, 6885-6893.
43. P. Horcajada, T. Chalati, C. Serre, B. Gillet, C. Sebrie, T. Baati, J. F. Eubank, D. Heurtaux, P. Clayette, C. Kreuz, J.-S. Chang, Y. K. Hwang, V. Marsaud, P.-N. Bories, L. Cynober, S. Gil, G. Ferey, P. Couvreur and R. Gref, *Nat Mater* **2010,** *9*, 172-178.
44. J. Hermannsdörfer, M. Friedrich, N. Miyajima, R. Q. Albuquerque, S. Kümmel and R. Kempe, *Angew. Chem. Int. Ed.***2012,** *51*, 11473-11477.
45. W. Cho, S. Park and M. Oh, *Chem. Commun.* **2011,** *47*, 4138-4140.

46. H. J. Lee, W. Cho, E. Lim and M. Oh, *Chem. Commun.* **2014,** *50*, 5476-5479.
47. L. He, Y. Liu, J. Liu, Y. Xiong, J. Zheng, Y. Liu and Z. Tang, *Angew. Chem. Int. Ed.* **2013,** *52*, 3741-3745.
48. Z. Dong, X. Le, Y. Liu, C. Dong and J. Ma, *J. Mater. Chem. A* **2014,** *2*, 18775-18785.
49. J. Liu, Z. Sun, Y. Deng, Y. Zou, C. Li, X. Guo, L. Xiong, Y. Gao, F. Li and D. Zhao, *Angew. Chem. Int. Ed.* **2009,** *121*, 5989-5993.
50. B. Li, H. Cao, J. Shao, M. Qu and J. H. Warner, *J. Mater. Chem.* **2011,** *21*, 5069-5075.
51. K. M. Mangold, J. Schuster and C. Weidlich, *Electrochim. Acta* **2011,** *56*, 3616-3619.
52. X. Gu, Z.-H. Lu, H.-L. Jiang, T. Akita and Q. Xu, *J. Am. Chem. Soc.* **2011,** *133*, 11822-11825.
53. T. Yao, T. Cui, X. Fang, F. Cui and J. Wu, *Nanoscale* **2013,** *5*, 5896-5904.
54. P. C. J. Graat and M. A. J. Somers, *Applied Surface Science* **1996,** *100–101* (0), 36-40.
55. J. Qu, L. Shi, C. He, F. Gao, B. Li, Q. Zhou, H. Hu, G. Shao, X. Wang and J. Qiu, *Carbon* **2014,** *66*, 485-492.
56. M. E. Compeán-Jasso, F. Ruiz, J. R. Martínez and A. Herrera-Gómez, *Mater. Lett.* **2008,** *62*, 4248-4250.
57. L. Zhou, Y. Shao, J. Liu, Z. Ye, H. Zhang, J. Ma, Y. Jia, W. Gao and Y. Li, *ACS Appl. Mat. Interfaces* **2014,** *6*, 7275-7285.
58. H.-j. Zhang, S.-d. Qi, X.-y. Niu, J. Hu, C.-l. Ren, H.-l. Chen and X.-g. Chen, *Catalysis Science & Technology* **2014,** *4*, 3013-3024.
59. L. Zhang, T. Lu, J. Bao, Y. Tang and C. Li, *Electrochem. Commun.* **2006,** *8*, 1625-1627.
60. X. Chen, Z. Cai, X. Chen and M. Oyama, *J. Mater. Chem. A* **2014,** *2*, 5668-5674.
61. Y. Xie, B. Yan, H. Xu, J. Chen, Q. Liu, Y. Deng and H. Zeng, *ACS Appl. Mat. Interfaces* **2014,** *6*, 7275-7285.
62. Y. Tang, T. Wu, B. Hu, Q. Yang, L. Liu, B. Yu, Y. Ding and S. Ye, *Mater. Chem. Phys.* **2015,** *149–150*, 460-466.

Figures and Tables

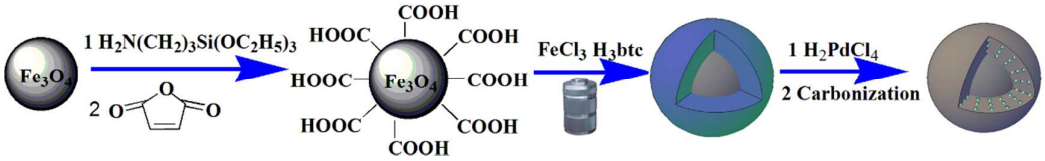

Fig. 1 Schematic illustration of the fabrication process of Fe_3O_4@MC-Pd microspheres.

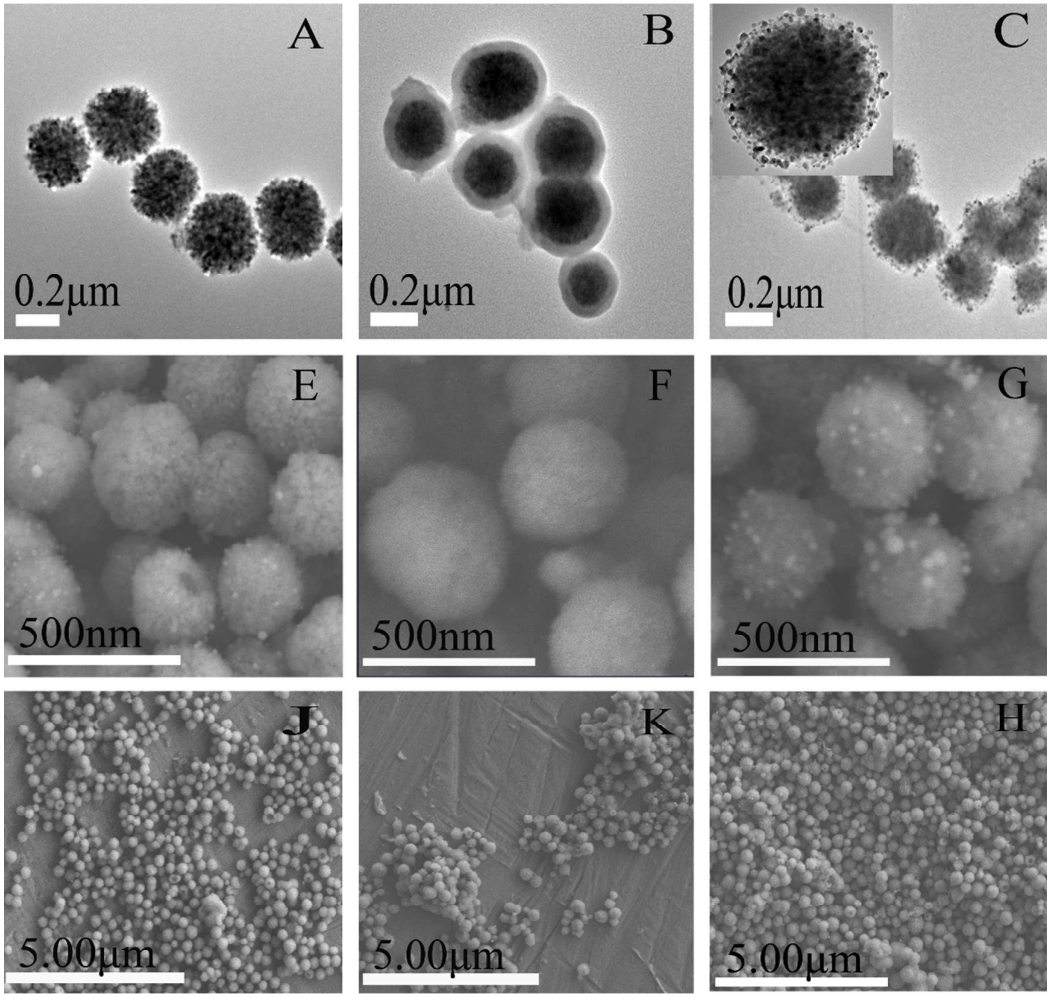

Fig. 2 TEM and SEM images of the Fe_3O_4(A, E, J), Fe_3O_4@MIL-100(B, F, K), Fe_3O_4@MC-Pd(C, G, H).

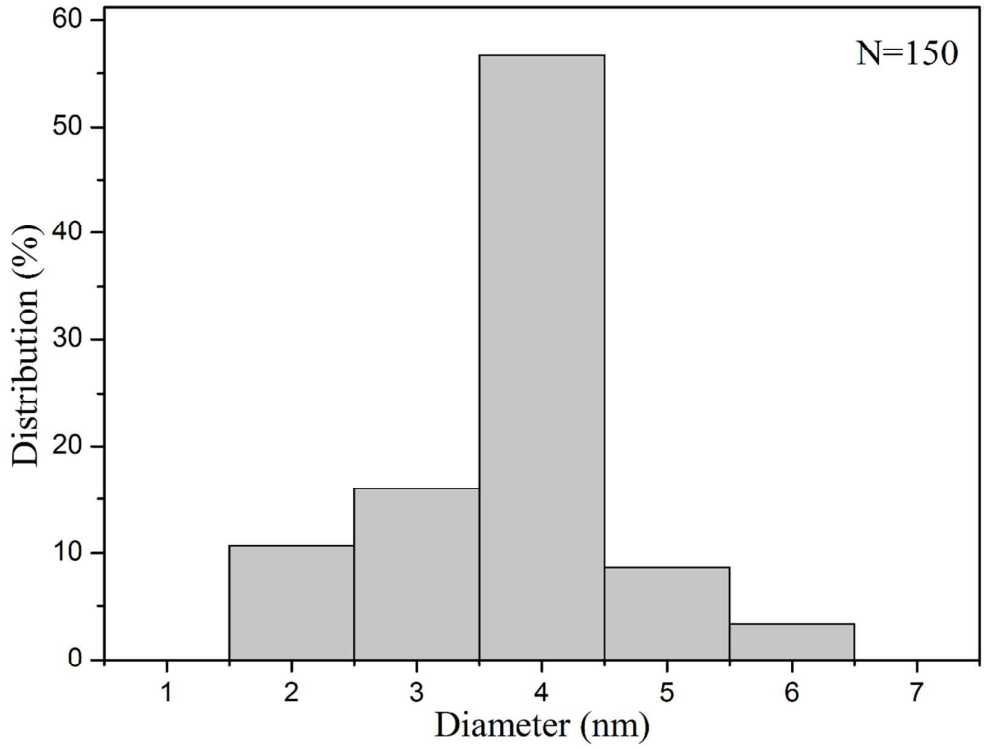

Fig. 3 size distribution of Pd nanoparticles on the surface of Fe_3O_4@MC-Pd.

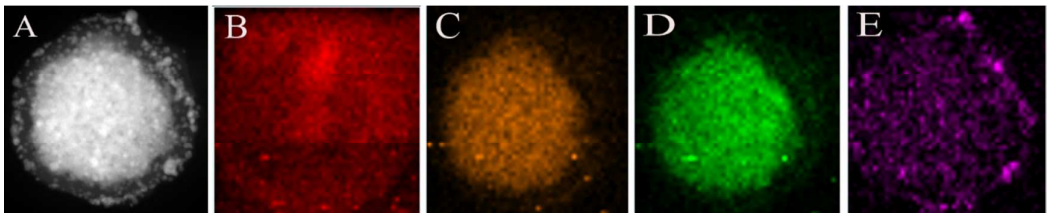

Fig. 4 HAADF-STEM image of (A) Fe_3O_4@MC-Pd, (B) C mapping image (C-K), (C) O mapping image (O-K), (D) Fe mapping image (Fe-L), (E) Pd mapping image (Pd-K).

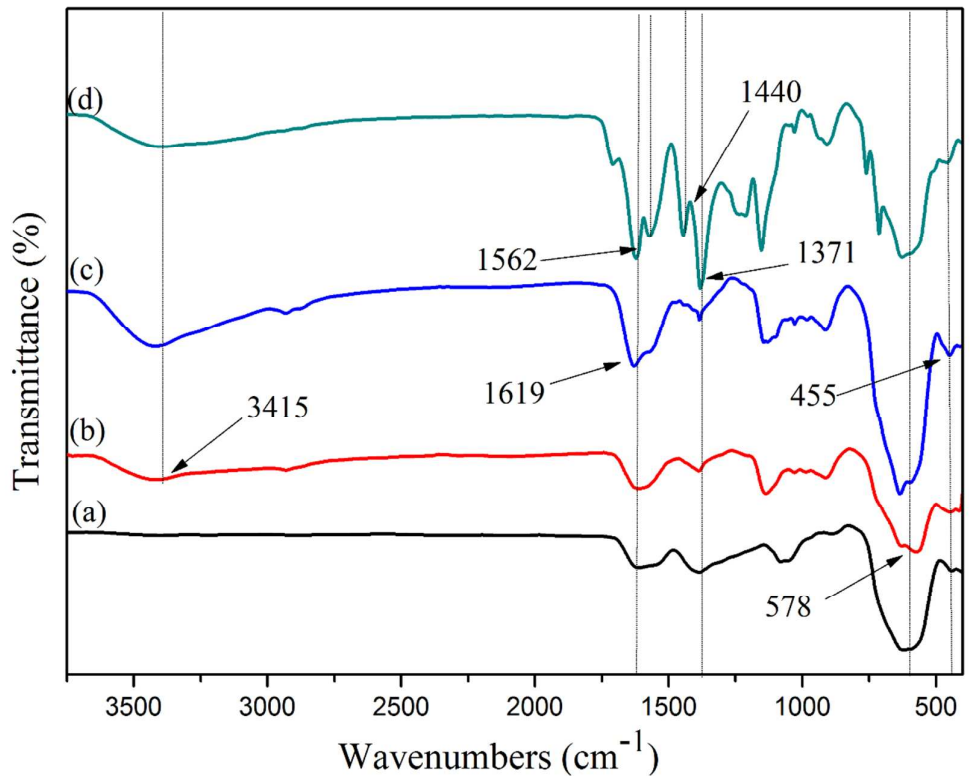

Fig. 5 FT-IR spectra of Fe_3O_4 (a), Fe_3O_4/APTES (b), Fe_3O_4/COOH (c) and Fe_3O_4@MIL-100 (d).

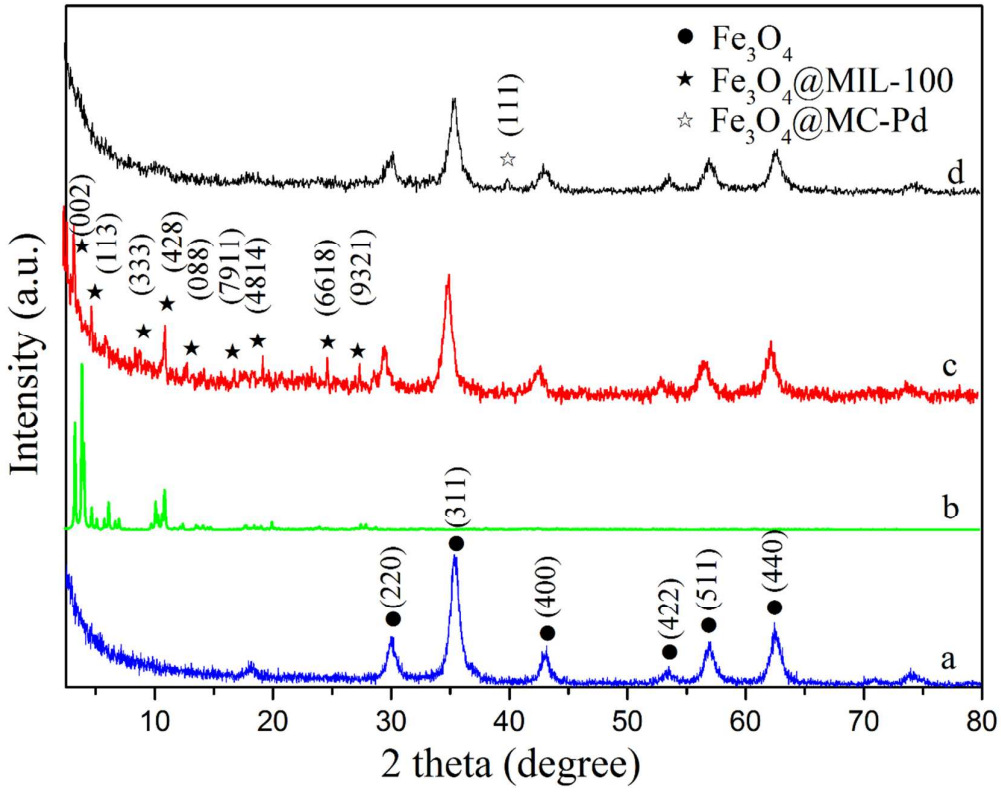

Fig. 6 XRD patterns of (a) Fe_3O_4, (b) the crystallographic data of MIL-100, (c) Fe_3O_4@ MIL-100, (d) Fe_3O_4@MC-Pd.

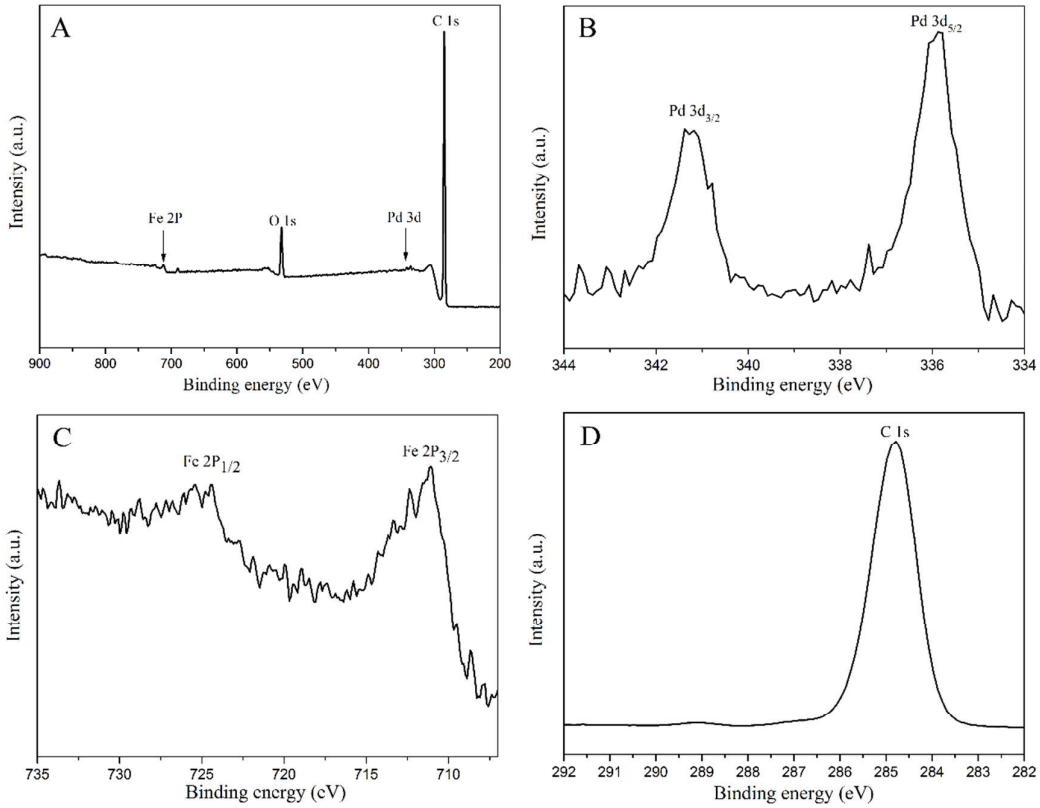

Fig. 7 XPS spectra of Fe_3O_4@MC-Pd: survey spectrum (A), high resolution of Pd spectrum (B), high resolution of Fe spectrum (C), and high resolution of C spectrum (D).

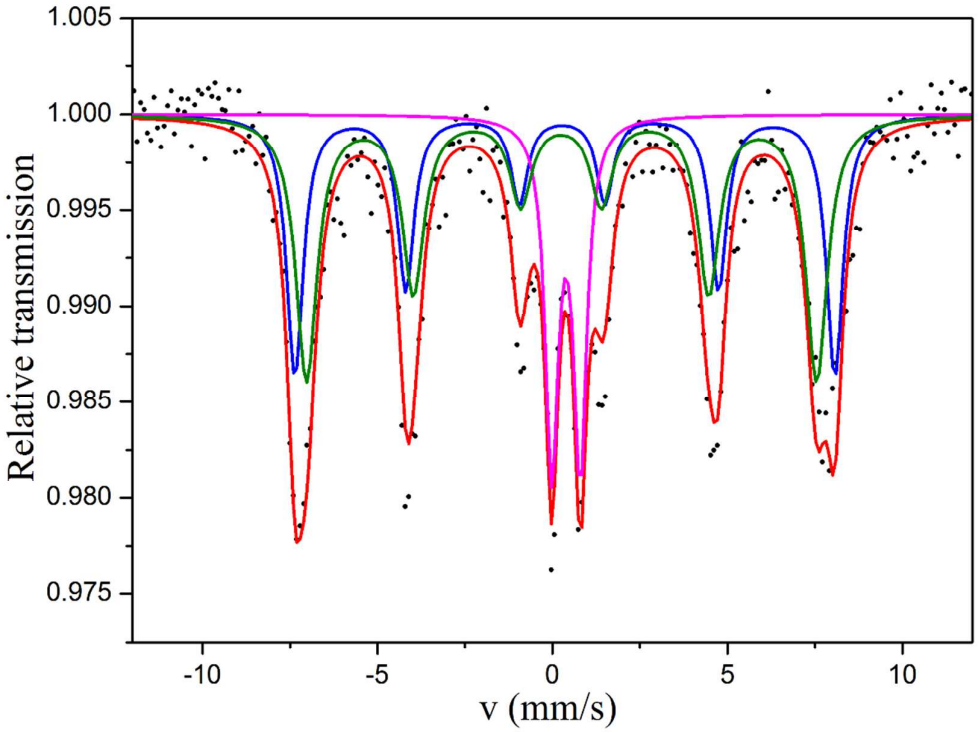

Fig. 8 Mössbauer spectrum of Fe_3O_4@MC-Pd

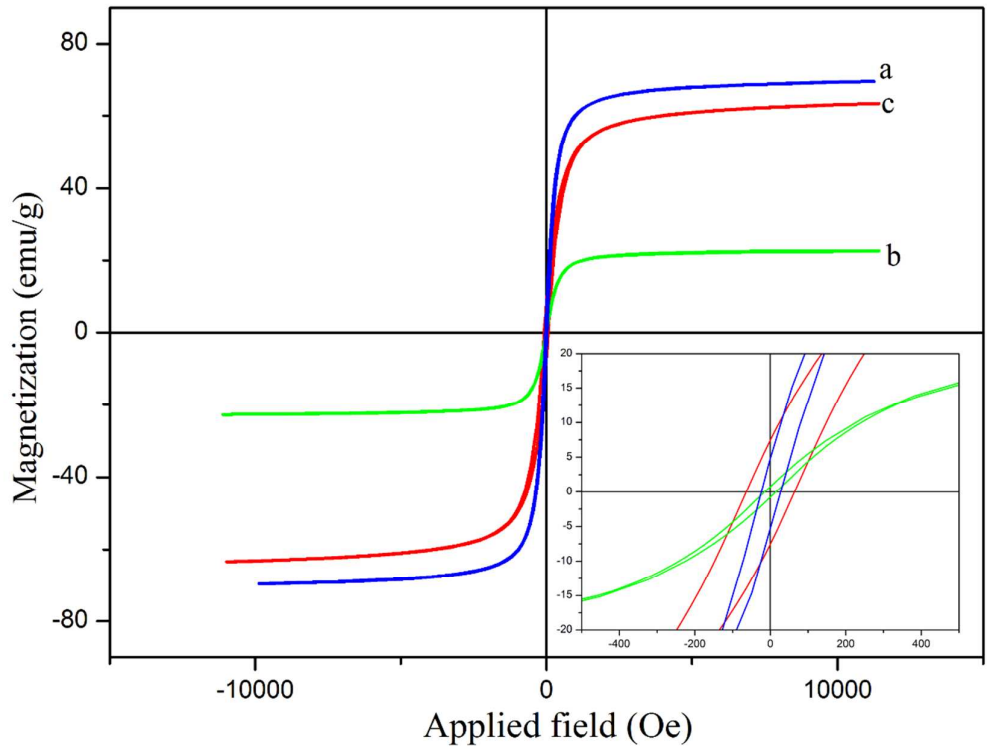

Fig. 9 Magnetic hysteresis loops of Fe_3O_4 (a), Fe_3O_4@MIL-100 (b) and Fe_3O_4@MC-Pd (c). The inset is a magnified view of the magnetization versus field

curves.

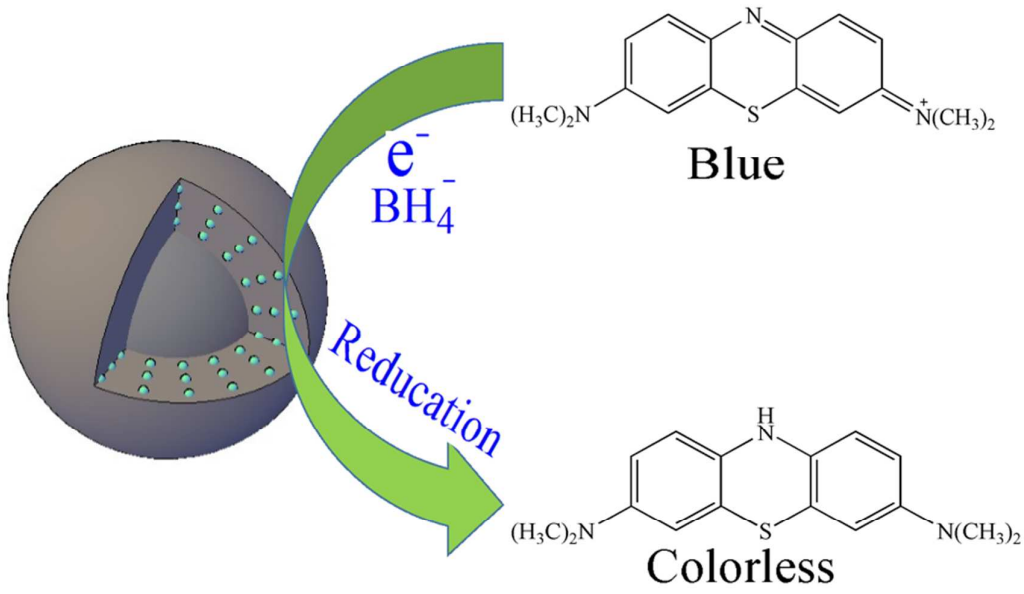

Fig. 10 Schematic of Fe_3O_4@MC-Pd microspheres as catalysts for the reduction of MB.

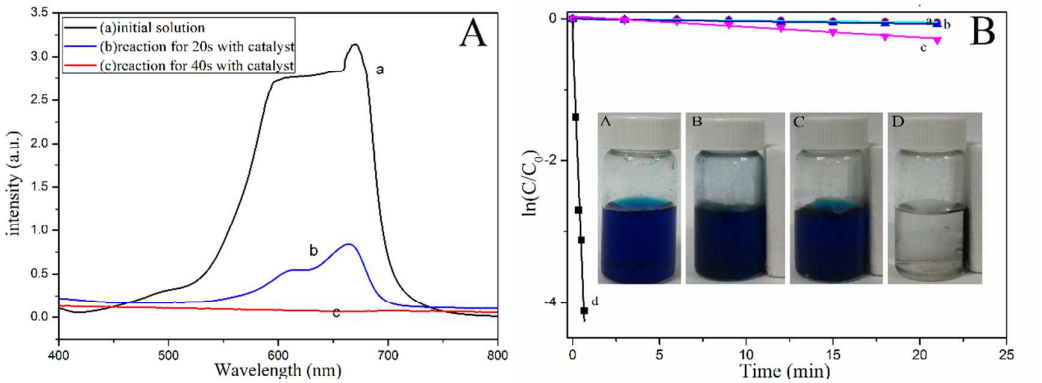

Fig. 11 (A) Time dependent absorption spectra for the catalytic reduction of MB by $NaBH_4$ in the presence of Fe_3O_4@MC-Pd catalyst. (B) The relationships of $\ln(C/C_0)$ versus reaction time plot in the presence of 10 mg different catalysts: (a) no catalysts, (b) Fe_3O_4, (c) Fe_3O_4@MC, (d) Fe_3O_4@MC-Pd. The inset indicate the colors of MB + $NaBH_4$ are different in the absence of catalyst (A) and in the presence of Fe_3O_4 (B), Fe_3O_4@MC (C) and Fe_3O_4@MC-Pd (D).

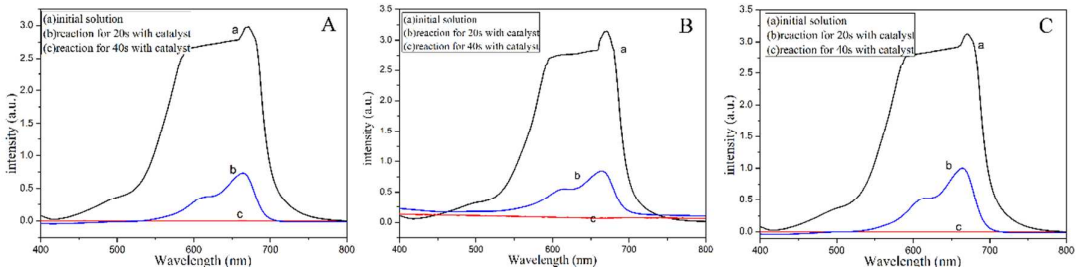

Figure 12. Successive UV−vis spectra for catalytic reduction of MB aqueous solution by $NaBH_4$ and Fe_3O_4@MC-Pd microspheres at (a) pH 3, (b) pH 7, and (c) pH 9.

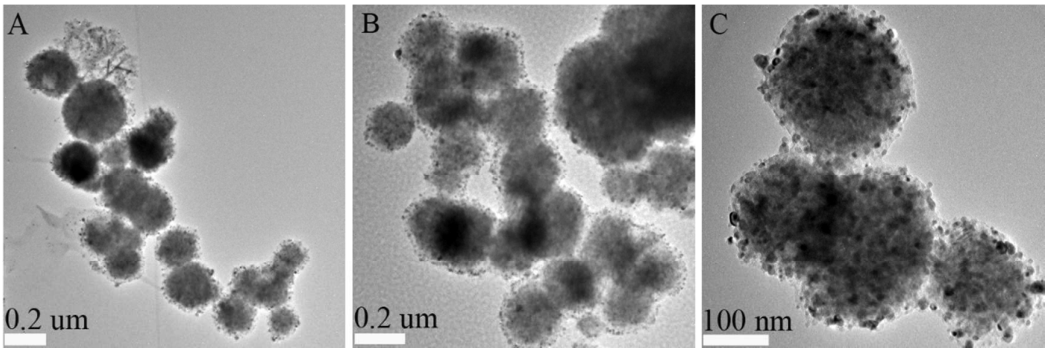

Fig. 13 TEM images of (A) Fe_3O_4@MC-Pd microspheres dispersed in boiling water for 10 h. (B) Fe_3O_4@ MC-Pd microspheres dispersed in acid solution with pH 2 for 24 h. (C) Fe_3O_4@ MC-Pd dispersed in alkali solution with pH 12 for 24 h.

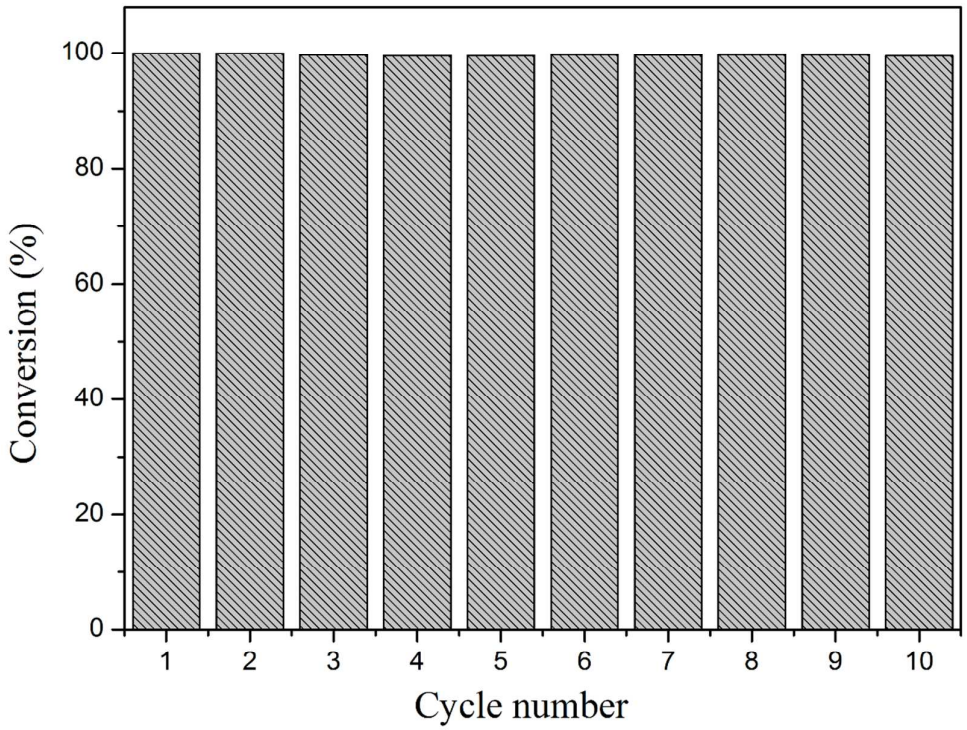

Fig. 14 The reusability of the as-prepared catalysts for the reduction of MB with $NaBH_4$.

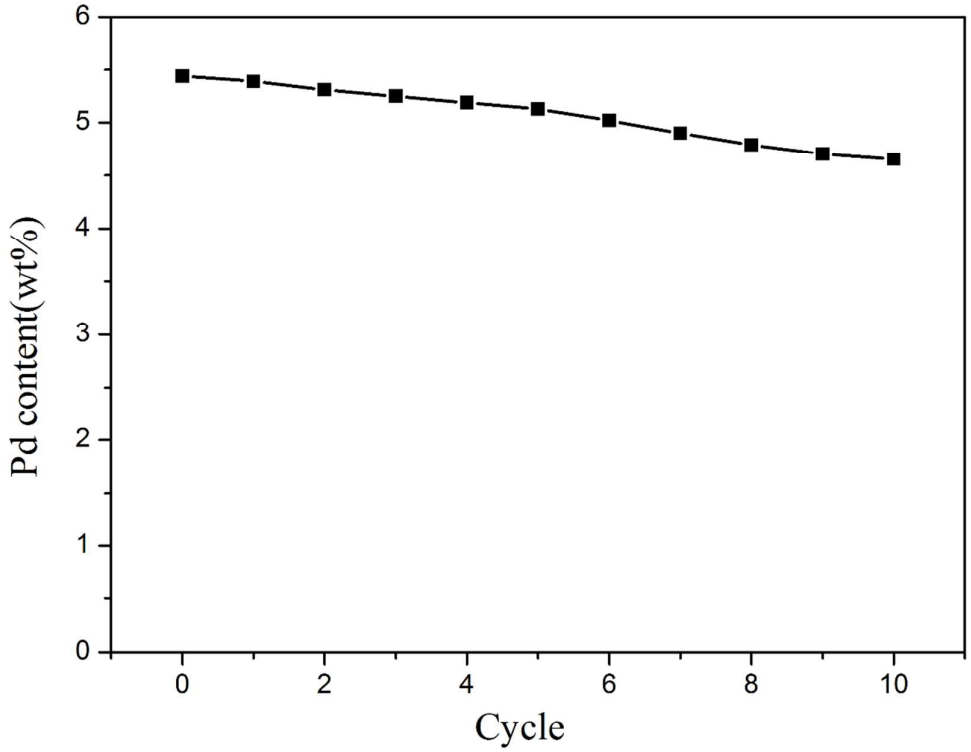

Fig. 15 Changes of Pd content after each cycle.

Table 1 Magnetic Properties of Fe_3O_4, Fe_3O_4@MIL-100 (Fe) and Fe_3O_4@MC-Pd

Samples	Magnetic Properties		
	M_S (emu/g)	H_C (Oe)	M_R (emu/g)
Fe_3O_4	69.5	27.6	4.8
Fe_3O_4@MIL-100 (Fe)	22.7	16.2	1.1
Fe_3O_4@MC-Pd	60.4	65.6	7.6

Table 2 ICP-AES Results of Fe_3O_4@MC-Pd under Acid and alkali Conditions

Entry	**Catalyst**	**Pd content (wt.%)**	**k (min^{-1})**
1	Fe_3O_4@MC-Pd	5.44	5.97
2	Fe_3O_4@MC-Pd (pH 2, 24 h)	5.27	5.74
3	Fe_3O_4@MC-Pd (pH 12, 24 h)	5.41	5.90